Tomographic image of the proton

R. Dupré[1], M. Guidal[1] & M. Vanderhaeghen[2]
[1]*Institut de Physique Nucléaire d'Orsay, CNRS-IN2P3, Université Paris-Sud, Université Paris-Saclay, 91406 Orsay, France.*
[2]*Institut für Kernphysik and PRISMA Cluster of Excellence, Johannes Gutenberg-Universität, Mainz, Germany.*

We determine, based on the latest experimental Deep Virtual Compton Scattering experimental data, the dependence of the spatial size of the proton on the quark's longitudinal momentum. This results in a three-dimensional momentum-space image and tomography of the proton.

PACS numbers:

arXiv:1606.07821v1 [hep-ph] 24 Jun 2016

More than 50 years after the discovery of the partonic substructure of the proton, the precise way in which the quarks and gluons compose the nucleon and build up its global properties, i.e. its mass, momentum, charge, or spin distributions is still not well-known and understood. The past two decades have seen an important progress both theoretically and experimentally in exploring proton structure through the $ep \to ep\gamma$ process, or Deeply Virtual Compton Scattering (DVCS). The angular and energy distributions of the scattered electron and radiated photon reflect both the momentum and space distributions of the quarks within the proton. In the present work, we perform a global analysis of recent DVCS data and extract the transverse extension of the proton for different longitudinal quark momentum slices.

The rigorous mathematical formalism for the quantitative interpretation of the DVCS process is based on QCD (Quantum Chromo-Dynamics). The process is illustrated in Fig. 1-left. The theory states that the process can be factorized between the elementary, precisely calculable, photon-quark Compton scattering and some universal structure functions, called Generalized Parton Distributions (GPDs), which encode the correlations in spatial and momentum distributions of the quarks in the proton. We refer the reader to Refs. [1–4] for the original articles on GPDs and to Refs. [5–9] for recent reviews of the field. The factorization for the DVCS process has been shown to hold for sufficiently large Q^2, the squared momentum transfer between the final and initial leptons, and sufficiently small $-t \ll Q^2$, the squared momentum transfer between the final and initial protons.

The GPDs are functions of three variables: x, ξ, and t. In a fast moving proton consisting of near-collinear partons, $x+\xi$ ($x-\xi$) represent the longitudinal momentum fractions of initial (final) quark w.r.t. the average nucleon momentum. The momentum transfer t is the conjugate variable of the localization of the quark in the transverse position plane, perpendicular to the proton momentum direction. An interpretation of GPDs thus emerges as distributions describing a quark being taken out of the proton with momentum fraction $x+\xi$ and being reinserted in the proton with momentum fraction $x-\xi$ at a given transverse distance.

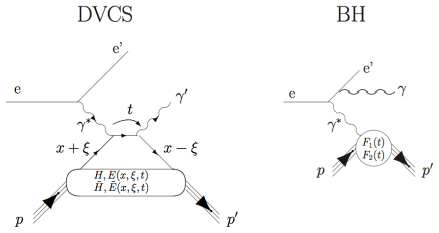

Figure 1: Left: the DVCS process (there is also a crossed diagram where the final state photon is emitted from the initial quark). Right: the BH process (there is also the process with final state photon emitted from the initial electron). The various variables and quantities are defined in the text.

Accessing GPDs from DVCS observables is a very challenging task. The first challenge results from the fact that in the QCD leading-twist framework in which this work is placed, there are four quark helicity-conserving GPDs, denoted by H, E, $\tilde{H}$, and $\tilde{E}$, entering the DVCS process.

A second challenge is that the GPDs actually enter the DVCS amplitude in a form where they are integrated over x. The observables thus depend on quantities which are functions of only the two kinematic variables ξ and t (neglecting Q^2 QCD-evolution effects, given the small Q^2 ranges dealt with in this work). These observables are called Compton Form Factors (CFFs) and are given for the GPD H by:

$$\begin{aligned} \mathcal{H}_{Re}(\xi,t) &\equiv \mathcal{P}\int_0^1 dx \left\{\frac{1}{x-\xi}+\frac{1}{x+\xi}\right\} H_+(x,\xi,t), \\ \mathcal{H}_{Im}(\xi,t) &\equiv H_+(\xi,\xi,t), \end{aligned} \quad (1)$$

where $\mathcal{P}$ denotes a principal value convolution integral. The so-called singlet GPD combination H_+ is defined as:

$$H^q_+(x,\xi,t) \equiv H^q(x,\xi,t) - H^q(-x,\xi,t). \quad (2)$$

The last complication arises from the fact that there is another significant mechanism contributing to the $ep\gamma$ final state. It is the Bethe-Heitler (BH) process, where the final state photon is radiated by the incoming or scattered electron. The process is illustrated in Fig. 1-right. The BH and DVCS mechanisms interfere at the amplitude

level. However, the BH amplitude is precisely calculable within Quantum Electrodynamics (QED). The only non-QED inputs in the calculation are the proton form factors (FFs) $F_1(t)$ and $F_2(t)$ and these are well-known at the small momentum transfers t considered in this work.

In Refs. [10–14], we proposed and applied a method to extract the CFFs from $ep\gamma$ observables. It consists in taking the eight CFFs as free parameters and, knowing the well-established BH and DVCS leading-twist amplitudes, to fit simultaneously with a least-square method, several $ep \to ep\gamma$ observables, at a fixed (ξ, t) kinematics. In general, an experimental observable receives contributions from several CFFs and there are important correlations between these. The extraction of eight CFFs from only a few observables, with finite experimental uncertainties, is thus in general an underconstrained problem. However, some observables are dominated and mostly sensitive to one or two CFFs. For instance, it is well-established that the beam-spin observables are dominated by the $\mathcal{H}_{Im}$ CFF. Then, if the range of variation of the CFFs is limited, the CFFs dominantly contributing to the observables can come out of the fit procedure with finite error bars. These error bars, defined by $\Delta\chi^2 = +1$ around the minimum χ^2 point, are then in general due to the correlations between the CFFs. Rather than the error of the experimental data, they reflect the influence of the other (subdominant) CFFs. Up to the limits imposed on the variation of the CFFs, which should be taken as conservatively as possible, this approach has the merit of being essentially model-independent as there is no need to assume and hypothesize any functional shape for the CFFs. This fitting method was applied, in our earlier works, to derive limits and constraints for the $\mathcal{H}_{Im}$, $\tilde{\mathcal{H}}_{Im}$ and $\mathcal{H}_{Re}$ CFFs at an average $\approx 40\%$ level for earlier $ep \to ep\gamma$ data from JLab [10, 11] and HERMES [12, 13].

Recently, the CLAS and Hall A collaborations of JLab, using a 5.75 GeV electron beam, have released new measurements of four observables of the $ep \to ep\gamma$ reaction: unpolarized cross sections, differences of beam-polarized cross sections (Hall A [15] and CLAS [16]), longitudinally polarized target single spin asymmetries and double spin asymmetries with both beam and longitudinal target polarizations (CLAS [17, 18]). These new data make up the largest set of $ep \to ep\gamma$ observables available to date in terms of kinematical coverage and binning. We have analyzed with the fitting approach outlined above simultaneously all these new data.

We focus here on the $\mathcal{H}_{Im}$ CFF which is the dominant contributor to the aforementioned JLab observables and which thus comes the most straightforwardly and systematically out of the fit with the smallest error bars. We show in Fig. 2 the results that we obtain at each (ξ, Q^2, t) bin, from the fit of the JLab CLAS data with 8 CFFs as free parameters. Like in our previous works, we have defined the range of variation of the CFFs as ± 5 times the CFFs given by the VGG model [5, 19–21]. Our fitting

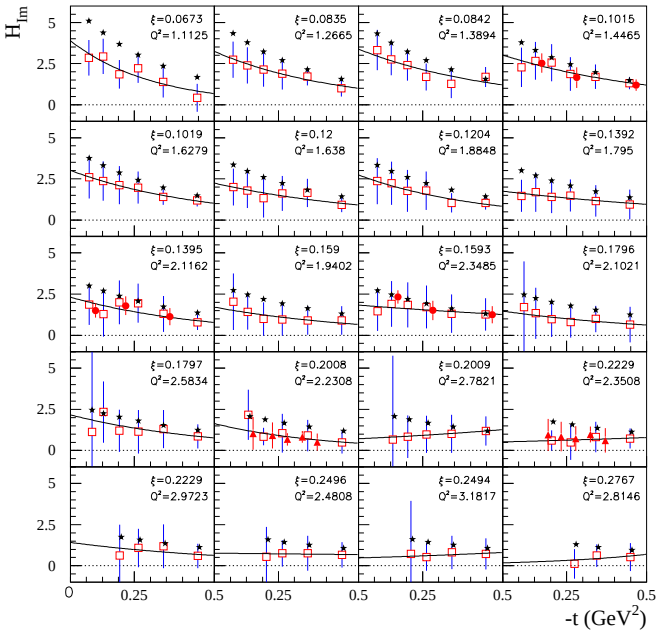

Figure 2: t-dependence of the CFF $\mathcal{H}_{Im}$ for 20 CLAS (x_B, Q^2) bins. Open squares: results of the CLAS σ and $\Delta\sigma$ fit, with the 8 CFFs as free parameters. Solid circles: results of the fit to CLAS σ and $\Delta\sigma$ data, as well as longitudinally polarized target and double beam-target polarized asymmetries, with the 8 CFFs as free parameters. Solid triangles: results of the Hall A σ and $\Delta\sigma$ fit with the 8 CFFs as free parameters. Stars: VGG reference CFFs. The solid curve shows an exponential fit of the open squares.

procedure has been checked at length and validated by numerous Monte-Carlo studies: we generated random 8-CFFs sets, calculated from them observables in a realistic way, i.e. smearing these pseudo-data so as to mimick the experimental resolution of the real data, fitted them by our least-square method with a series of random starting values for the CFFs in order to be biased by particular initial conditions, and finally compared the results to the originally generated CFF values. The intensive technical Monte-Carlo studies will be detailed in a more detailed methodological article to come.

In Fig. 2, the results of the fit of the CLAS σ and $\Delta\sigma$ data are shown by the empty squares. For a few (ξ, Q^2, t) bins, longitudinally polarized target and double beam-target polarized asymmetries from the CLAS experiment are also available at approximately the same kinematics as the data for σ and $\Delta\sigma$. We show the values of $\mathcal{H}_{Im}$ obtained from the simultaneous fit of these 4 observables with the solid circles. The solid circles have smaller error bars than the empty squares as expected, since additional observables in the fit obviously bring new constraints. We also added in Fig. 2 the result of the fits of σ and $\Delta\sigma$

from Hall A, where there is overlap with the CLAS data. There is in general a good agreement between the $\mathcal{H}_{Im}$ values extracted from both experiments. For reference, we show in Fig. 2 the predictions of the VGG model. The comparison shows that the version of the VGG model that has been taken for the reference CFF (corresponding with $b_v = b_s = 1$) tends to overestimate the data at small values of t by around 30 %.

We observe the general trend that $\mathcal{H}_{Im}$ decreases with t and that these t-slopes tend to become steeper as ξ decreases. We have quantified this and extracted a general (ξ, t)-dependence of the CFFs, by fitting the t-dependence with an exponential function as given by:

$$\mathcal{H}_{Im}(\xi, t) = A(\xi) e^{B(\xi) t}. \quad (3)$$

The solid lines in Fig. 2 show the results of these exponential fits of the empty squares.

In Fig. 3, we plot the dependence of both the amplitude A and the exponential t-slope B on ξ. In spite of the large size of the errors, which are not statistical we recall, one can observe that, systematically, both A and B tend to increase as ξ decreases. Physically, at small ξ, one expects A to to rise steeply as $1/\xi$ due to the sea-quark contribution. Furthermore, A is expected to vanish in the limit $\xi \to 1$, when one valence quark takes all longitudinal momentum. Therefore, we fit A by the simple one-parameter form which embodies both features:

$$A(\xi) \;=\; a_A(1-\xi)/\xi, \quad (4)$$

and will extract the parameter a_A from a fit to the data. For the slope B, we expect it to sharply decrease from a Regge type behavior when $\xi \to 0$ to a flat t-dependence in the limit $\xi \to 1$, reflecting the pointlike coupling to a valence quark carrying all longitudinal momentum. To encompass both limits, we fit the slope B by the following one-parameter ansatz in ξ:

$$B(\xi) = a_B \ln(1/\xi). \quad (5)$$

The rise of B at small ξ corresponds to the increase of the transverse size of the proton as smaller longitudinal momentum fractions are probed. A fit to the data with the functional forms of Eqs. (4, 5) yields the values:

$$a_A = 0.36 \pm 0.06, \quad a_B \;=\; 1.07 \pm 0.26 \text{ GeV}^{-2}. \quad (6)$$

The resulting fits are shown by the bands in Fig. 3.

We can confront the experimentally extracted values of A and B with the expectations from GPD models, as shown in Fig. 3. We compare two GPD models: the dual model [22] and the VGG double distribution (DD) model [5, 19–21]. For the latter, we use three choices of the valence (sea) profile parameters b_v (b_s) respectively. For large values of these profile parameters ($b \to \infty$), the GPD $H(x, \xi, t)$ tends to the GPD $H(x, 0, t)$, where the effect of the skewness (ξ-dependence) disappears. For the

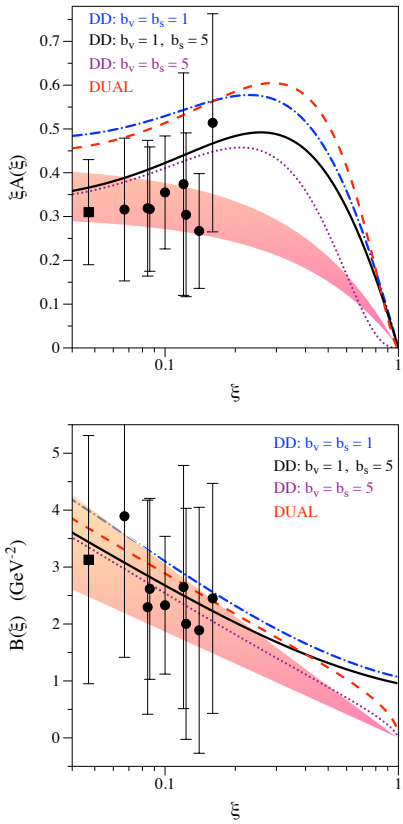

Figure 3: Upper: Amplitude A of $\mathcal{H}_{Im}$, multiplied by ξ, as a function of ξ. Lower: t-slope B of $\mathcal{H}_{Im}$ as a function of ξ. Data points: 8 CFFs fit of data corresponding with 4 observables from JLab/CLAS (circles), and from HERMES (square) the latter as extracted in Refs. [9, 12]. For the JLab points, we kept only the 8 lowest ξ bins of Fig. 2 which provide the lowest uncertainty results. The one-parameter fits to these data points according to Eqs. (4, 5) are shown by the bands, corresponding with a 1σ variation of a_A and a_B, given by Eq. (6). The theory curves correspond with the dual model and the double distribution (DD) model for three choices of the valence (sea) profile parameters b_v (b_s), as indicated.

dual model, we have used the lowest forward-like function. For both models, we use the same empirical forward parton distributions as input and use in both cases a Regge parameterization for the t-dependence with slope parameter 1.05 GeV^{-2}, see Ref. [9] for details.

Comparing the extracted data for A with theory, we notice from Fig. 3 that in the region $0.05 \lesssim \xi \lesssim 0.2$ the data tend to lie systematically below the result of the dual model (with lowest forward-like function), as well as the DD models where sea quarks have strong skewness ($b_s = 1$). The DD models with small skewness effects of sea-quarks ($b_s = 5$) are in good agreement with the data. To distinguish for the valence quarks between the cases of strong skewness ($b_v = 1$) and weak skewness ($b_v = 5$) will require data in the region $\xi \gtrsim 0.3$. We also notice

from Fig. 3 that the GPD models predict a maximum for $\xi A(\xi)$ around $\xi \approx 0.3$, due to the x-dependence of the underlying valence quark distributions.

In the lower panel of Fig. 3, we show the exponential t-slope $B(\xi)$, as a function of ξ. We notice that all GPD models, which are based on a Regge parameterization for its t-dependence, are in good agreement with the available data for B. Both the data as well as the models follow a $\ln(1/\xi)$ behavior, thus leading to an increase of the slope as ξ decreases. Only for $\xi \gtrsim 0.5$, some qualitative differences between the models appear.

We now seek to relate the increasing t-slope $B(x)$ when x decreases with the variation of the spatial size of the proton when probing partons with different longitudinal momentum fraction x. For this purpose, we relate it to the (helicity averaged) transverse charge distribution in the proton, denoted by ρ, which is obtained through a 2-dimensional Fourier transform of the FF F_1 as [23]:

$$\rho(\mathbf{b}_\perp) = \int \frac{d^2\mathbf{\Delta}_\perp}{(2\pi)^2} e^{-i\mathbf{b}_\perp\cdot\mathbf{\Delta}_\perp} F_1(-\mathbf{\Delta}_\perp^2), \tag{7}$$

where $\mathbf{b}_\perp$ denotes the quark position in the plane transverse to the longitudinal momentum of a fast moving proton, and $\mathbf{\Delta}_\perp$ denotes the transverse components of the momentum transferred to the proton. The squared radius of the unpolarized 2-dimensional transverse charge distribution in the proton is then defined as:

$$\langle b_\perp^2 \rangle = \int d^2\mathbf{b}_\perp \mathbf{b}_\perp^2 \rho(\mathbf{b}_\perp). \tag{8}$$

The quantity $\langle b_\perp^2 \rangle$ is related to the conventionally defined squared radius $\langle r_1^2 \rangle$ of the proton FF F_1 as $\langle b_\perp^2 \rangle = 2/3 \langle r_1^2 \rangle$. The experimental value of $\langle r_1^2 \rangle$ based on elastic electron-proton scattering data yields [24]: $\langle r_1^2 \rangle = 0.65 \pm 0.01$ fm^2, resulting in the empirical value for the proton's transverse squared radius:

$$\langle b_\perp^2 \rangle = 0.43 \pm 0.01 \text{ fm}^2 = 11.05 \pm 0.26 \text{ GeV}^{-2}. \tag{9}$$

Similarly to the FFs, the t variable in the GPDs is the conjugate variable of the impact parameter. For $\xi = 0$ (for which $t = -\Delta_\perp^2$), one therefore has an impact parameter version of GPDs through a Fourier integral in $\Delta_\perp$, which for a parton of flavor q reads as :

$$\rho^q(x, \mathbf{b}_\perp) = \int \frac{d^2\mathbf{\Delta}_\perp}{(2\pi)^2} e^{-i\mathbf{b}_\perp\cdot\mathbf{\Delta}_\perp} H_-^q(x, 0, -\mathbf{\Delta}_\perp{}^2). \tag{10}$$

Here $H_-^q(x,0,t)$ is the so-called non-singlet or valence GPD combination, defined as:

$$H_-^q(x,0,t) \equiv H^q(x,0,t) + H^q(-x,0,t), \tag{11}$$

with $0 \le x \le 1$. At ξ=0, the function $\rho^q(x, \mathbf{b}_\perp)$ can then be interpreted as the number density of quarks of flavor q with *longitudinal* momentum fraction x at a given *transverse* distance $\mathbf{b}_\perp$ in the proton [23]. Generalizing Eq. (8), one can define the x-dependent squared radius of this quark density in the transverse plane as:

$$\langle b_\perp^2 \rangle^q(x) = \frac{\int d^2\mathbf{b}_\perp \mathbf{b}_\perp^2 \rho^q(x, \mathbf{b}_\perp)}{\int d^2\mathbf{b}_\perp \rho^q(x, \mathbf{b}_\perp)}, \tag{12}$$

which can be expressed through the GPD H_- as:

$$\langle b_\perp^2 \rangle^q(x) = -4 \frac{\partial}{\partial \mathbf{\Delta}_\perp^2} \ln H_-^q(x, 0, -\mathbf{\Delta}_\perp{}^2) \Big|_{\mathbf{\Delta}_\perp = 0}. \tag{13}$$

Assuming the t-dependence of the valence GPD $H_-^q(x,0,t)$ to be exponential of the form:

$$H_-^q(x,0,t) = q_v(x) e^{B_0(x)t}, \tag{14}$$

with $q_v(x)$ the corresponding valence quark distribution, Eq. (13) then yields for each flavor q:

$$\langle b_\perp^2 \rangle^q(x) = 4 B_0(x). \tag{15}$$

The x-independent squared radius is obtained from $\langle b_\perp^2 \rangle^q(x)$ through the following average over x:

$$\langle b_\perp^2 \rangle^q = \frac{1}{N_q} \int_0^1 dx\, q_v(x)\, \langle b_\perp^2 \rangle^q(x), \tag{16}$$

with the integrated number of valence quarks $N_u = 2$ and $N_d = 1$. For the proton, the Dirac squared radius $\langle b_\perp^2 \rangle$ is then obtained as the charge weighted sum over the valence quarks: $\langle b_\perp^2 \rangle = 2e_u \langle b_\perp^2 \rangle^u + e_d \langle b_\perp^2 \rangle^d$, with quark electric charges $e_u = +2/3$ and $e_d = -1/3$. A Regge ansatz for the t-slope of $H_-^q(x,0,t)$ yields:

$$B_0(x) = a_{B_0} \ln(1/x), \tag{17}$$

with a_{B_0} the Regge slope. When evaluating the corresponding integral of Eq. (16), using the empirical constraint of Eq. (9) for $\langle b_\perp^2 \rangle$, we obtain the estimate:

$$a_{B_0} = (1.05 \pm 0.02)\, \text{GeV}^{-2}. \tag{18}$$

To quantitatively compare this with the t-slope of $\mathcal{H}_{Im}$ defined through Eq. (3), we need to be aware of a difference. The experimentally measured t-slope $B(x)$ is for the singlet GPD combination $H_+(x,x,t)$. On the other hand, the t-slope $B_0(x)$ of Eq. (17, 18) is for the valence GPD in the limit $\xi = 0$, i.e. for the function $H_-^q(x,0,t)$ for a quark of flavor q. In our analysis, we assume that the function $B_0(x)$ is the same for u and d quarks, in agreement with the observed universality of the Regge slopes for meson trajectories. To get some quantitative idea how large the difference between the (flavor independent) slopes B_0 and B is, we have studied the x-dependence of the ratio $B_0(x)/B(x)$ within both the dual and DD GPD models. For the x range of the available data, $0.05 \lesssim x \lesssim 0.2$, we notice that the GPD models with $b_s = 5$, which were found to be compatible with

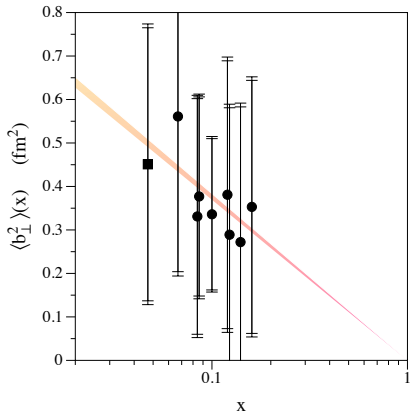

Figure 4: x-dependence of $\langle b_\perp^2 \rangle$ for quarks in the proton. The band shows the empirical result using the logarithmic ansatz for $B_0(x)$ of Eqs. (17, 18). The data points correspond with the results obtained in this work for $B(x)$, as displayed in Fig. 3. They have been multiplied by the correction factor $B_0/B \simeq 0.925 \pm 0.025$ in the x-range of the data. The resulting (small) model uncertainty is shown by the outer error bars.

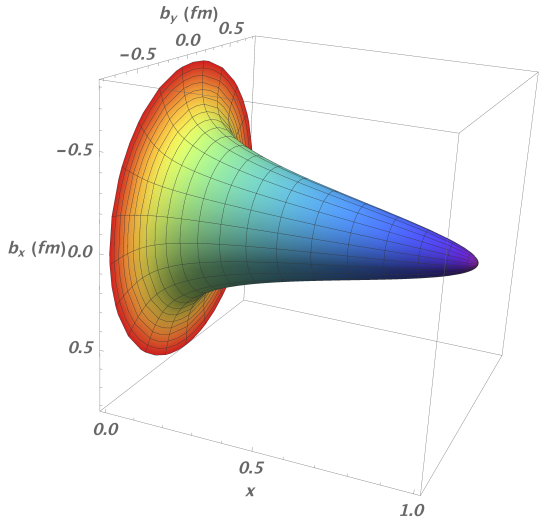

Figure 5: x-dependence of the proton's transverse extent obtained from the data of Fig. 4.

both the data for A and B, yield: $0.90 < B_0/B < 0.95$. As a result, we can convert the data for $B(x)$ to data for $\langle b_\perp^2 \rangle(x)$ using Eq. (15), as shown in Fig. 4. They are compared with the result using the logarithmic ansatz for $B_0(x)$ of Eq. (17), with parameter a_B determined from the proton Dirac radius. One sees that within errors both determinations are perfectly compatible. We have here extracted the x-dependence of the squared radius of the quark distributions in the transverse plane, demonstrating an increase of this radius with decreasing value of the longitudinal quark momentum fraction x. Fig. 5 shows a three-dimensional view of the numerical function that we obtained by the fit of the data of Fig. 4.

In summary, we have analyzed in a GPD QCD leading-twist and leading-order framework the latest $ep \to ep\gamma$ unpolarized cross sections, difference of beam-polarized cross sections, longitudinally polarized target single spin, and beam-longitudinally polarized target double spin asymmetries recently measured at JLab. We have extracted constraints on the $\mathcal{H}_{Im}$ CFF over a large range in ξ. From the amplitude and the t-slope of $\mathcal{H}_{Im}$, we have been able to derive a functional mapping of the density and transverse size of the proton charge as a function of the quark's longitudinal momentum.

Acknowledgments

We are very thankful to S. Niccolai and D. Mueller for very useful discussions. R.D. and M.G. benefitted from the ANR-12-MONU-0008-01 "PARTONS" contract support. The work of M.V. was supported in part by the Deutsche Forschungsgemeinschaft DFG through the Collaborative Research Center SFB 1044.

[1] X. Ji, Phys. Rev. Lett. **78**, 610 (1997).
[2] D. Mueller, D. Robaschik, B. Geyer, F. M. Dittes and J. Horejsi, Fortsch. Phys. **42**, 101 (1994).
[3] A.V. Radyushkin, Phys. Lett. B **380**, 417 (1996).
[4] X. Ji, Phys. Rev. D **55**, 7114 (1997).
[5] K. Goeke, M.V. Polyakov and M. Vanderhaeghen, Prog. Part. Nucl. Phys. **47**, 401 (2001).
[6] M. Diehl, Phys. Rept. **388**, 41 (2003).
[7] A.Belitsky and A.Radyushkin, Phys.Rept. **418**, 1 (2005).
[8] S. Boffi and B. Pasquini, Riv. Nuovo Cim. **30**, 387 (2007).
[9] M. Guidal, H. Moutarde and M. Vanderhaeghen, Rept. Prog. Phys. **76**, 066202 (2013).
[10] M. Guidal, Eur. Phys. J. A **37**, 319 (2008) [Erratum-ibid. A **40**, 119 (2009)];
[11] M. Guidal, Phys. Lett. B **689**, 156 (2010).
[12] M. Guidal and H. Moutarde, Eur.Phys.J.A **42**, 71 (2009).
[13] M. Guidal, Phys. Lett. B **693**, 17 (2010).
[14] M. Boër and M. Guidal, J. Phys. G **42** 3, 034023 (2015).
[15] M. Defurne *et al.* [Jefferson Lab Hall A Coll.], Phys. Rev. C **92** 5, 055202 (2015).
[16] H. S. Jo *et al.* [CLAS Coll.], Phys. Rev. Lett. **115**, 212003 (2015).
[17] S. Pisano *et al.* [CLAS Coll.], Phys. Rev. D **91** 5, 052014 (2015).
[18] E. Seder *et al.* [CLAS Coll.], Phys. Rev. Lett. **114** 3, 032001 (2015) [Phys. Rev. Lett. **114** 8, 089901 (2015)].
[19] M. Vanderhaeghen, P.A.M. Guichon and M. Guidal, Phys. Rev. Lett. **80** 5064 (1998).
[20] M. Vanderhaeghen, P.A.M. Guichon and M. Guidal, Phys. Rev. D **60**, 094017 (1999).
[21] M. Guidal, M.V. Polyakov, A.V. Radyushkin and M. Vanderhaeghen, Phys. Rev. D **72**, 054013 (2005).
[22] M. V. Polyakov and M. Vanderhaeghen, arXiv:0803.1271 [hep-ph].

[23] M. Burkardt, Phys. Rev. D **62**, 071503 (2000).
[24] J. C. Bernauer *et al.* [A1 Coll.], Phys. Rev. C **90**, 1, 015206 (2014).